

# Objective Assessment of Sonographic Quality I: Task Information

Nghia Q. Nguyen, Craig K. Abbey, and Michael F. Insana\*

**Abstract**—In this paper, we explore relationships between the performance of the ideal observer and information-based measures of class separability in the context of sonographic breast-lesion diagnosis. This investigation was motivated by a finding that, since the test statistic of the ideal observer in sonography is a quadratic function of the echo data, it is not generally normally distributed. We found for some types of boundary discrimination tasks often required for sonographic lesion diagnosis, the deviation of the test statistic from a normal distribution can be significant. Hence the usual relationships between performance and information metrics become uncertain. Using Monte Carlo studies involving five common sonographic lesion-discrimination tasks, we found in each case that the detectability index  $d_A^2$  from receiver operating characteristic analysis was well approximated by the Kullback–Leibler divergence  $J$ , a measure of clinical task information available from the recorded radio-frequency echo data. However, the lesion signal-to-noise ratio,  $\text{SNR}_I^2$ , calculated from moments of the ideal observer test statistic, consistently underestimates  $d_A^2$  for high-contrast boundary discrimination tasks. Thus, in a companion paper, we established a relationship between image-quality properties of the imaging system and  $J$  in order to predict ideal performance. These relationships provide a rigorous basis for sonographic instrument evaluation and design.

**Index Terms**—Breast imaging, detectability, ideal-observer analysis, image quality, Kullback–Leibler divergence.

## I. INTRODUCTION

**I**MAGING systems are devices that transport information from objects being examined to observers of the image who make decisions. Wagner [1] approached the assessment of data quality by first partitioning the image formation process into *acquisition* and *display* stages (Fig. 1). The sonographic acquisition stage, where patient information is recorded as radio-frequency (RF) echo signals, is governed by instrumentation variables including pulse transmission and echo reception properties up to and including beamforming. The sonographic dis-

play stage includes any postsummation data filtering, envelope detection, scan conversion, and gray-scale mapping leading to final B-mode presentation.

The performance of the imaging system depends fundamentally on the task, i.e., the reason for acquiring data. We can measure task performance at either stage of image formation by calculating the scalar-valued test statistic of the *ideal observer* [2]. That calculation requires expression of the visual task in terms of the likelihood functions. Likelihood functions are conditional probability densities defining two data classes; e.g., normal and abnormal. By tracking the information at different stages of image formation, losses can be evaluated and the instruments are reconfigured to maximize information transfer [3]–[6].

Wagner and Brown [3] proposed the system performance metric  $\text{SNR}_I$ , the signal-to-noise ratio for the ideal observer, which is composed of moments of the test statistic. They expanded  $\text{SNR}_I^2$  for low-contrast tasks into a Fourier basis that separated properties of the instrumentation from the diagnostic features. Their integral expression for  $\text{SNR}_I^2$  included a quantity known as the *noise equivalent quanta (NEQ)* that is composed of frequency-dependent factors defining contrast resolution, spatial resolution, and acquisition noise. Further, in situations where the test statistic is normally distributed,  $\text{SNR}_I^2$  equals the detectability index  $d_A^2$  found from the area under the receiver operating characteristic (ROC) curve (AUC) of the ideal observer. Thus, ideal task-based performance became predictable by measuring the sensitivity of the instrument in the spatial frequency channels of a diagnostic feature. These relationships allow imaging systems to be designed to maximize delivery of specific clinical information, and they form the foundation for medical image quality assessments [2], [7].

Smith *et al.* [8] applied similar approaches to display-stage sonography to derive an ideal observer test statistic for low-contrast lesion detection in B-mode imaging. To manage the non-linear display-stage processes, stringent limiting assumptions were imposed to find  $\text{SNR}_I^2$  in the image domain. The assumptions included no acquisition noise, shift-invariant focal-zone impulse responses, and speckle spot sampling rather than pixel sampling, which limited the analysis to the detection of large-area low-contrast lesions. They discovered how properties of the transducer, lesion contrast, and speckle influence lesion detectability. Their ideal-observer analysis of B-mode image data guided subsequent work in speckle reduction [9], beamformation [10], and postprocessing [11].

As an alternative to working in the echo-envelope domain of the display stage, we have applied the ideal-observer approach to the study of RF echo signals in acquisition-stage sonography (Fig. 1) [12]–[14]. RF echo-signal analysis is practical since

Manuscript received October 20, 2012; revised December 02, 2012; accepted December 03, 2012. Date of publication December 11, 2012; date of current version March 29, 2013. This work was supported by the National Institutes of Health (NIH) under Award CA118294. *Asterisk indicates corresponding author.*

N. Q. Nguyen is with the Department of Electrical and Computer Engineering, University of Illinois at Urbana-Champaign, Urbana, IL 61801 USA and also with the Earth and Environmental Science Division, Los Alamos National Laboratory, Los Alamos, NM 87544 USA (e-mail: nghia@lanl.gov).

C. K. Abbey is with the Department of Psychology, University of California, Santa Barbara, CA 93106 USA (e-mail: craig.abbey@psych.ucsb.edu).

\*M. F. Insana is with the Department of Bioengineering, Beckman Institute of Advanced Science and Technology, University of Illinois at Urbana-Champaign, Urbana, IL 61801 USA (e-mail: mfi@illinois.edu).

Color versions of one or more of the figures in this paper are available online at <http://ieeexplore.ieee.org>.

Digital Object Identifier 10.1109/TMI.2012.2232303

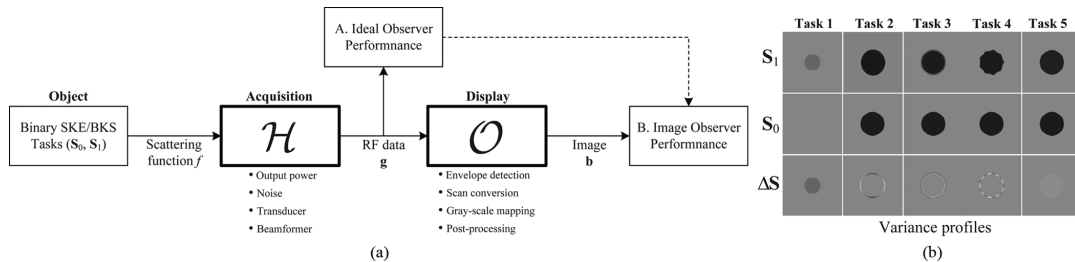


Fig. 1. (a) Illustration of sonographic system model and image quality assessment analysis. We study binary decision tasks where the signal (lesion-feature contrast) is known exactly (SKE) and the random background (speckle and acquisition noise) is known statistically (BKS). Instrument properties that influence the acquisition and display components of the imaging system are listed. (b) Variance profiles are shown for five visual tasks, including low-contrast detection (Task 1), eccentricity (Task 2), hard/soft boundary (Task 3), spiculation (Task 4), and hypoechoic/anechoic (Task 5).  $S_i$  specifies lesion contrast and geometry, while  $\Delta S = \sigma_{\text{obj}}^2(S_1 - S_0)$  indicates the task contrast.

many systems provide users with RF echo frames. More fundamentally, acquisition-stage analysis enables the use of linear-system models that reduce the limiting assumptions required in B-mode analysis. Measuring observer performance at both stages has allowed us to track the efficiency of information flow through the entire image formation process [12]–[14].

The goal of this paper is to define task information for breast sonography and find its relationship to ideal-observer performance. These results are the motivation for further study, in a companion paper [15], where we derive a spatial-frequency-domain expression analogous to NEQ that forms a basis for sonographic system design and objective evaluation.

## II. IDEAL OBSERVER AND PERFORMANCE METRICS

This section briefly summarizes the components used to define the performance of the ideal observer at simple two-class discrimination tasks. These components are applied in later sections to derive a link between performance and the Kullback–Liebler divergence, an information-theoretic measure of class separability. Additional background on the application of ideal-observer analysis to sonography can be found in previous publications [8], [12], [14].

### A. Echo Models

Vector  $\mathbf{g}$  represents all of the RF echo data from one 2-D image frame. For the purpose of this work, it consists of sampled scan lines created by beamforming over each transmit/receive sub-aperture, all concatenated into a single column vector for computational convenience. The RF data are modeled as a noisy linear transformation of a 2-D scattering object. We will represent the continuous object function by a set of sampled points  $\mathbf{f}$ , also arranged as a column vector, under the assumption that this spatial sampling is well above the pass band of the imaging system. The RF echo signal is related to the object through a noisy linear system [17]

$$\mathbf{g} = \mathbf{H}\mathbf{f} + \mathbf{n} \quad (1)$$

where  $\mathbf{H}$  is the imaging system matrix and vector  $\mathbf{n}$  represents signal-independent acquisition errors in the RF echo signal. The  $j$ th element of  $\mathbf{n}$  is modeled as zero-mean white Gaussian noise with distribution  $n_j \sim \mathcal{N}(0, \sigma_n^2)$ . The acquisition noise variance is adjusted to produce an echo signal-to-noise ratio,  $\text{SNR}_0$ , of 32 dB in the background regions surrounding lesion features.

With  $M$  total RF signal samples and  $N$  total object function samples,  $\mathbf{H}$  is  $M \times N$  with rows composed of shifted pulse-echo spatial sensitivity functions and columns composed of the associated point-spread functions [17]. In this study, the pulse-echo impulse responses are generated using Field II acoustic simulation software [18], [19] from parameters selected to model a 1-D linear array on the Siemens Antares system [20]. For computational convenience, the impulse response is assumed to be shift invariant throughout the frame. A B-mode image vector  $\mathbf{b}$  is produced when nonlinear display-stage operator  $\mathcal{O}$  is applied to the echo signal,  $\mathbf{b} = \mathcal{O}\mathbf{g}$ [17]. Dimensions of  $\mathbf{b}$  and  $\mathbf{g}$  are usually different, and  $\mathbf{b}$  is reordered to form a 2-D image array for viewing.

### B. 2-D Features and Discrimination Tasks

Physicians look for specific sonographic features when detecting and diagnosing cancerous breast lesions [16]. For simulation studies designed to optimize signal acquisition and processing, we have developed a panel of simple visual tasks based on the features used to detect and classify malignant and benign masses. Each feature imposes different statistical properties on the object vector  $\mathbf{f}$ , as described below, depending on whether it is a member of the malignant or benign class. Task 1 requires detection of a low-contrast hypoechoic lesion, and Tasks 2–5 involve discriminating subtle features representing low- and high-contrast lesions [see Fig. 1(b)].

Task difficulty is controlled by changing the feature parameter associated with each task. For example, in Task 1 the feature parameter controls the reduction in scattering intensity within a fixed lesion area. When this parameter is increased, a more obvious hypoechoic lesion is simulated, resulting in higher detection performance. Observers are made fully aware of all visual task features.

### C. Object Contrast

In this section, we briefly explain why object contrast in pulse-echo sonography is modeled as a zero-mean random field with a variance that changes spatially according to the backscatter intensity [23]. As compressional ultrasound waves travel through glandular breast tissues, most of the wave energy is absorbed. A small portion of the transmitted pulse energy is backscattered at *surfaces* of tiny regions in tissue where the acoustic impedance varies. The scattered waves energy is coherently detected by the transducer and beamformed to give

g. Tissue structures of greatest interest for lesion discrimination are the microvasculature, cell nuclei, and extracellular protein fibers composed of collagen and elastin [21]. Many of these structures are poorly organized and smaller than the ultrasonic wavelength, and thus soft tissues are often modeled as diffuse, weakly-scattering random media (Rayleigh scatterers) that generate incoherent backscatter [22]. Sonographic contrast is generated locally as the disease process modifies the size and density of tissue scatterers and/or interstitial fluid pressure.

In reality, tissues also contain specular and other coherent scattering components that we recognize in sonograms as gross anatomical features. We assume in our study that the backscattered energy from these components is negligible compared with the incoherent scattering energy.

We model breast lesions in 2-D as areas of lower scatterer number density (smaller object variance) within a uniformly scattering background. For object scattering function  $f(x, y)$ , the geometric shape of a simulated lesion is generated by multiplying a spatially uniform variance by a lesion-feature template,  $S(x, y)$ , such as those illustrated in Fig. 1(b). Mathematically, we have  $f(x, y) = \mathcal{N}(0, \sigma_{\text{obj}}^2) \times \sqrt{1 + S(x, y)}$ , which is rearranged to form column vector  $\mathbf{f}$ . The covariance matrix for a nonstationary, multivariate-normal object vector  $\mathbf{f} = \text{MVN}(\mathbf{0}, \mathbf{\Sigma}_{\text{obj}})$  is  $\mathbf{\Sigma}_{\text{obj}} = \sigma_{\text{obj}}^2(\mathbf{I} + \mathbf{S})$ , where  $\mathbf{I}$  is the identity matrix and  $\mathbf{S}$  is a diagonal matrix rearrangement of  $S(x, y)$  sampled at the same points as the object. Lesion shape and contrast are defined by  $\mathbf{S}$ . To generate the two classes of data needed for observer testing, we generate  $\mathbf{S}_0$  and  $\mathbf{S}_1$  to represent, respectively, the benign and malignant features diagrammed in Fig. 1(b) for five tasks related to lesion diagnosis.

#### D. Ideal Observer

Since  $\mathbf{g}$  represents one frame of the RF echo data recorded from  $\mathbf{f}$ , the covariance matrix of  $\mathbf{g}$  is found by passing  $\mathbf{\Sigma}_{\text{obj}}$  through the linear imaging operator and adding acquisition noise. For the  $i$ th class of data, where  $i = 0, 1$ , we find

$$\mathbf{\Sigma}_i = \mathbf{H}\mathbf{\Sigma}_{\text{obj}}\mathbf{H}^t + \mathbf{\Sigma}_n = \sigma_{\text{obj}}^2\mathbf{H}(\mathbf{I} + \mathbf{S}_i)\mathbf{H}^t + \sigma_n^2\mathbf{I}. \quad (2)$$

Denoting the MVN echo-data density  $p_i(\mathbf{g}) \triangleq p(\mathbf{g}|i)$ , where

$$p(\mathbf{g}|i) = \frac{1}{(2\pi)^{M/2} \det \mathbf{\Sigma}_i} \exp \left[ -\frac{1}{2} \mathbf{g}^t \mathbf{\Sigma}_i^{-1} \mathbf{g} \right]$$

the ideal observer operating on  $\mathbf{g}$  of unknown class is given by the log-likelihood ratio [2]

$$\lambda(\mathbf{g}) = \ln \left( \frac{p_1(\mathbf{g})}{p_0(\mathbf{g})} \right). \quad (3)$$

Reducing (3) and eliminating terms unrelated to  $\mathbf{g}$  because they do not modify discrimination performance, it was shown that [12]

$$\lambda(\mathbf{g}) = \frac{1}{2} \mathbf{g}^t (\mathbf{\Sigma}_0^{-1} - \mathbf{\Sigma}_1^{-1}) \mathbf{g}. \quad (4)$$

This scalar test statistic is quadratic in  $\mathbf{g}$  [24] because the task feature is encoded in covariances  $\mathbf{\Sigma}_i$  via  $\mathbf{S}_i$ . Superscript  $t$  denotes vector/matrix transpose.

In the two-alternative forced choice (2AFC) experiments used in our study, two sets of data are presented to the observer

at the same time;  $\mathbf{g}'$  is drawn from  $p_0(\mathbf{g})$  and  $\mathbf{g}''$  from  $p_1(\mathbf{g})$  [2]. Equation (4) is used to compute  $\lambda(\mathbf{g}')$  and  $\lambda(\mathbf{g}'')$ , and the larger of the two values is assigned class  $i = 1$ . The decision is correct when  $\lambda(\mathbf{g}'') \geq \lambda(\mathbf{g}')$  and otherwise incorrect.

#### E. Performance Metrics

Let  $q_i(\lambda) \triangleq q(\lambda(\mathbf{g})|i)$  represent the probability density of  $\lambda$  when class  $i$  is true. In Monte Carlo evaluations, these densities are estimated from histograms of the measurements obtained after a power series is applied to (4) to compute the inverse covariance matrices. The degree of overlap between  $q_0(\lambda)$  and  $q_1(\lambda)$  is one measure of the separability between  $p_0(\mathbf{g})$  and  $p_1(\mathbf{g})$ . The probabilities of detection  $P_D(t)$  and false alarm  $P_F(t)$  at decision threshold  $\lambda = t$  are functions of  $q_i(\lambda)$  [25]

$$\begin{aligned} P_D(t) &= \Pr(\lambda(\mathbf{g}) > t | i = 1) = \int_t^\infty d\lambda q_1(\lambda) \\ P_F(t) &= \Pr(\lambda(\mathbf{g}) > t | i = 0) = \int_t^\infty d\lambda q_0(\lambda). \end{aligned} \quad (5)$$

An ROC curve plots  $P_D$  as a function of  $P_F$  for all threshold values  $t$ . Noting that  $dP_F(t)/dt = -q_0(t)$  and  $P_F \rightarrow (0, 1)$  as  $t \rightarrow (\infty, -\infty)$ , the area under the ROC curve is [6]

$$\text{AUC} = \int_{-\infty}^\infty dt q_0(t) P_D(t). \quad (6)$$

AUC is the probability that randomly drawn values of  $\lambda$ , given that the signal is present, will be larger than those when the signal is absent. It is a scalar with values between 0.5 and 1.0, and it equals the proportion of correct responses  $P_c$  resulting from a 2AFC experiment [25]. An observer adopting the ideal strategy of (4) will maximize AUC to achieve maximum discrimination performance [2]. Another measure of class separability, suggested by Wagner and Brown, is the signal-to-noise ratio for the ideal observer [3] that is obtained from moments of  $\lambda$

$$\text{SNR}_I^2 = \frac{(E_1\{\lambda\} - E_0\{\lambda\})^2}{(\text{var}_1\{\lambda\} + \text{var}_0\{\lambda\})/2} \quad (7)$$

where  $E_i\{\lambda\}$  and  $\text{var}_i\{\lambda\}$  are the means and variances of  $\lambda$  conditioned on data class  $i$  being true.  $\text{SNR}_I$  is labeled detectability index  $d'$  in the psychophysical literature [7], [25].

Detectability index  $d_A$ , however, is defined directly from AUC using the expression [6]

$$d_A = 2\text{erf}^{-1}(2\text{AUC} - 1) \quad (8)$$

where  $\text{erf}(\cdot)$  denotes the error function and  $\text{erf}^{-1}(\cdot)$  is its inverse. Under normality, the three metrics are simply related,  $\text{SNR}_I = d_A = 2\text{erf}^{-1}(2\text{AUC} - 1)$ , but over difference ranges,  $0.5 \leq \text{AUC} \leq 1$  corresponds to  $0 \leq d_A, \text{SNR}_I \leq \infty$  [7].  $d_A$  is defined the same way for non-normal  $q_i(\lambda)$  since  $d_A$  remains monotonic with AUC, but its interpretation as a signal-to-noise ratio may be compromised depending on the degree of deviation from normality.

For sonography, (4) shows that  $\lambda(\mathbf{g})$  has a quadratic form  $\mathbf{g}^t(\mathbf{\Sigma}_0^{-1} - \mathbf{\Sigma}_1^{-1})\mathbf{g}$ . The distributions  $q_i(\lambda)$  are difficult to characterize other than to say they are the difference between two correlated generalized- $\chi^2$  distributions each with  $k$  degrees-of-

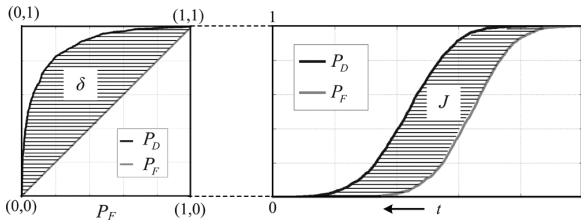


Fig. 2. (Left) The ROC curve displays  $P_D$  as a function of  $P_F$ . The shaded area is  $\delta = \text{AUC} - 0.5$ . (Right) Corresponding plots of  $P_D$  and  $P_F$  are shown as functions of the decision threshold  $\lambda = t$ . The area between these two curves equals the Kullback–Leibler divergence,  $J$ . These data are from one of the Monte Carlo studies displayed in Fig. 3.

freedom [24], [26]. Applying the central-limit theorem to a generalized  $\chi^2$  distribution, the rule of thumb is that it will approximate a normal distribution when  $k > 50$ . We do not have a rule for  $q_i(\lambda)$  except to say each is approximately normal when there are many independent data samples within the feature region to be detected.

### III. TASK INFORMATION

Our intuition leads us to believe that performance and class separability are related. It should be possible to predict the performance of the ideal observer for quadratic tasks based on the information contained in echo data  $\mathbf{g}$  if class separability is a surrogate for  $d_A^2$ .

The *Kullback–Leibler divergence*  $J$  quantifies the expected information in  $\mathbf{g}$  needed to discriminate in favor of one class over the other [28].  $J$  is an information measure of class separability. It makes no assumptions about the forms of  $p_i(\mathbf{g})$  or  $q_i(\lambda)$ , and we will show that it equals  $d_A^2$  under normality.  $J$  is a scalar SNR-like quantity defined as [31]

$$J \triangleq \int d\mathbf{g} (p_1(\mathbf{g}) - p_0(\mathbf{g})) \ln \left( \frac{p_1(\mathbf{g})}{p_0(\mathbf{g})} \right) = E_1\{\lambda(\mathbf{g})\} - E_0\{\lambda(\mathbf{g})\} \quad (9)$$

where the integration is over the sample space of the data.

To relate  $J$  and AUC, we show in Appendix A that for the ideal observer defined in (3)

$$J = \int_{-\infty}^{\infty} dt [P_D(t) - P_F(t)]. \quad (10)$$

This equation offers a graphical approach to measuring  $J$  from ideal-observer responses whenever  $P_D(t)$  and  $P_F(t)$  can be found. Consider Fig. 2 that illustrates (10) and compares that area with another area  $\delta \triangleq \text{AUC} - 0.5$ . Both plots, which are generated from the same measurement data, show areas that increase with greater class separability and both depend on  $P_D(t)$  and  $P_F(t)$ . From (6), it is straightforward to show that

$$\delta = \text{AUC} - 0.5 = \int_{-\infty}^{\infty} dt q_0(t) [P_D(t) - P_F(t)]. \quad (11)$$

Comparing (10) and (11), we see that the relationship between  $J$  and AUC depends on  $q_0(\lambda)$ . Areas  $\delta$  and  $J$  each quantify task information but in different coordinate systems.

The relationship between  $J$  and AUC is simple if  $q_0(t)$  is a normal density. Barrett [6] showed that if  $q_i(\lambda)$  is normal for

either class, the other must be normal with the same variance. Further  $E_1\{\lambda\} = -E_0\{\lambda\}$ ,  $\text{var}_0\{\lambda\} = \text{var}_1\{\lambda\} = 2E_1\{\lambda\}$ . By using a Taylor series expansion of  $J$ , we show in Appendix B that the normality condition allows  $J$  to be expressed in terms of moments of  $\lambda$

$$J = \frac{(E_1\{\lambda\} - E_0\{\lambda\})^2}{\frac{1}{2}(\text{var}_1\{\lambda\} + \text{var}_0\{\lambda\})} \quad (12)$$

which reduces to (9) when you apply the Barrett relations stated above (12). From (8), we find that normality ensures that

$$\sqrt{J} = \text{SNR}_I = d_A = 2 \text{erf}^{-1}(2\delta) = 2 \text{erf}^{-1}(2\text{AUC} - 1). \quad (13)$$

These relations hold for any imaging modality where a test statistic derived from likelihood ratios is normally distributed. When normality cannot be assumed, the relationship between AUC and  $J$  may still be determined, but numerically using (10). In the next section, we conduct Monte Carlo studies involving the five breast-lesion tasks described in Section II-B and Fig. 1(b). From those data, we compare performance metrics  $J$ ,  $d_A^2$ , and  $\text{SNR}_I^2$  to probe the effects of deviations from normal on their agreement.

### IV. MONTE CARLO STUDIES

#### A. Numerical Results

The main challenge to calculating  $J$  from (9) is computing matrix inverses and determinants. Many of the difficulties are avoided using (10), since determinants enter the expressions for  $P_D$  and  $P_F$  as additive constants in the log-likelihood ratios. Their influence is to shift both curves in Fig. 2 (right) along  $t$  by the same interval, and therefore they do not affect the area calculation.

$J$ ,  $d_A^2$ , and  $\text{SNR}_I^2$  were each estimated numerically from 2AFC observer studies. Studies included simulations of 2000 realizations of echo-data pairs generated per contrast for each task. Histograms of  $\lambda(\mathbf{g}')$  and  $\lambda(\mathbf{g}'')$  composed from the 2000 measurements formed estimates of  $q_0(\lambda)$  and  $q_1(\lambda)$ , respectively.  $d_A^2$  was computed from AUC by applying (8).  $\text{SNR}_I^2$  was found from moments of  $\lambda$  via (7), and  $\lambda$  was found from (4) using up to 250 terms in the series expansions of  $\Sigma_i^{-1}$  so that values converged within 0.001%.  $J$  was computed numerically from (10) using  $P_D(t)$  and  $P_F(t)$  that were estimated from histograms of  $\lambda$ . To control for case variability, we used the same RF echo data pairs to calculate the three figures of merit at each feature contrast. Plots of the results for the five tasks are found in Fig. 3.

We tested the significance of differences among metrics  $d_A^2$ ,  $\text{SNR}_I^2$  and  $J$  as follows. First we assumed AUC follows a binomial distribution, where  $n = 2000$ ,  $p = P_c = 0.8$ , so that the standard error is about 2% of the mean value  $(1-p)/\sqrt{n} \simeq 0.018$ . The corresponding standard errors in  $d_A^2$  are about 3% for  $\text{AUC} = P_c = 0.8$  as found by combining the information above with (8). For each task, the range  $0.5 \leq \text{AUC} \leq 0.99$  corresponded to  $0 \leq d_A^2 \leq 10.82$ ; we avoided  $\text{AUC} = 1$  since  $d_A^2 \rightarrow \infty$ . Not knowing the error distributions for  $J$  and  $\text{SNR}_I^2$ , we applied bootstrapping methods [29] (resampling with

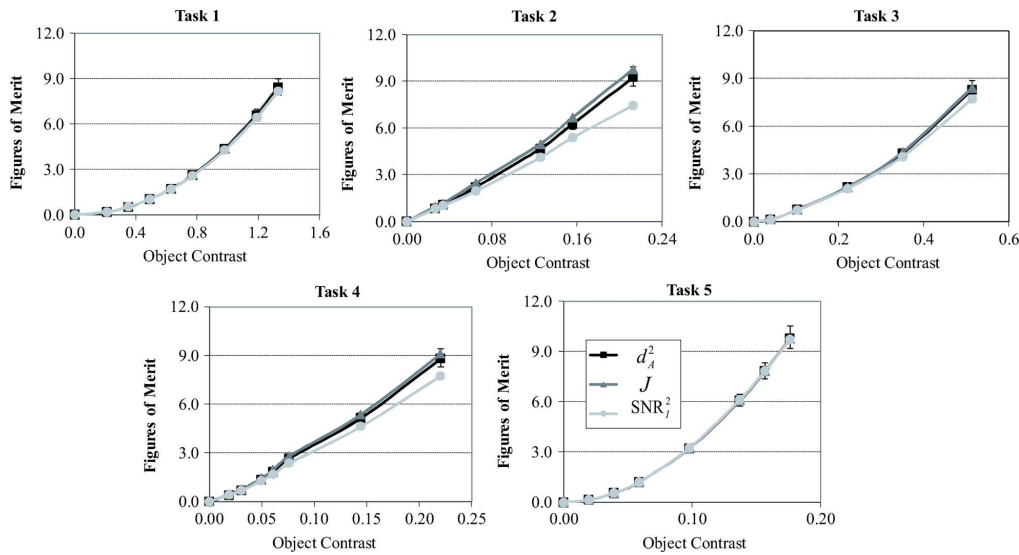


Fig. 3. Comparisons of metrics  $J$ ,  $d_A^2$ , and  $\text{SNR}_I^2$  for the five visual tasks illustrated in Fig. 1. Each of the three curves in a graph are plotted as a function of task contrast. The legend in the plot of Task 5 applies to all plots. Error bars indicate  $\pm$ one standard error.

replacement) to the ideal-observer 2AFC responses to estimate the corresponding standard errors for  $n_{\text{boot}} = 300$ . From means and standard errors of the three metrics, we computed their 95% confidence intervals. Two metrics are considered equivalent when their confidence intervals overlap.

Fig. 3 results show that the three metrics are clearly equivalent for large-area Tasks 1 and 5. Consequently, in these cases,  $q_i(\lambda)$  are well represented by a normal density. In Tasks 2 – 4, however,  $\text{SNR}_I^2$  diverges from  $J$  and  $d_A^2$  with differences up to 14.5% for Task 2. Although the metrics are statistically equivalent for Task 3, agreement is at the limits of the criteria. Task areas, displayed in Fig. 1(b) as  $\Delta S$ , are largest for Tasks 1 and 5, smallest for Tasks 2 and 4, and in between for Task 3. In all five tasks,  $J$  values are statistically equivalent to  $d_A^2$ . We attribute observed differences to sampling and numerical integration errors. Thus for the visual tasks considered,  $d_A^2$  is more closely approximated by  $J$  than  $\text{SNR}_I^2$ .

### B. Normality Condition

Test-statistic normality plays a central role in equating task information with observer performance. When densities  $p_i(\mathbf{g})$  are normal, the imaging operator  $\mathbf{H}$  is linear, and  $\lambda(\mathbf{g})$  is a linear function of  $\mathbf{g}$ , e.g., in standard mammography, the resulting test statistic density  $q_i(\lambda)$  is normal and the performance metric relations of (13) hold. In common sonographic situations,  $p_i(\mathbf{g})$  is normal,  $\mathbf{H}$  is a linear operator, but  $\lambda(\mathbf{g})$  is a quadratic function of  $\mathbf{g}$ , which results in  $q_i(\lambda)$  being generally non-normal. Nevertheless from the data of Fig. 3 we see that for large-area tasks, those where the feature area is large compared to the average speckle-spot area, the central-limit theorem applies and  $q_i(\lambda)$  are approximately normal. In boundary discrimination tasks 2 and 4, where task areas are smallest, there are too few independent data samples provided to the ideal observer to assume the central-limit theorem applies. In that situation, we found that  $\text{SNR}_I^2$  underestimates ideal performance given by  $d_A^2$ .

To demonstrate the effects of task area on normality, we repeated the Monte Carlo experiments of Fig. 3 twice; in Experi-

ment 1, lesion contrast was reduced and feature area increased to roughly maintain similar overall performance via AUC. In Experiment 2, lesion contrast was increased as feature area decreased. For example, a larger feature area in Task 2 is obtained by greater elliptical eccentricity in  $S_1$ , and, in Task 4, each simulated spiculation in  $S_1$  is longer. In Experiment 1, we expect the three metrics to be exactly equivalent since larger task areas increase the degrees-of-freedom over that found in the data of Fig. 3. In Experiment 2, we expect the performance metrics will diverge more than in Fig. 3 as smaller task areas reduce the degrees-of-freedom. Note that *lesion contrast*, defined as  $\max S_0$ , is fixed within an experiment but different between the two experiments, while *task contrast*, which is proportional to  $\Delta S$ , remains an independent variable as indicated in the plots.

The results of both experiments are displayed in Fig. 4. Experiment 1 results are shown in the top row (low lesion contrast, large task-contrast area). The three metrics tightly converge for both tasks, and a histogram of the test statistic results for class 0 data appears to fit a normal pdf (quantile–quantile plots are linear with correlation coefficient  $r^2 = 0.9996$ ). Experiment 2 results (high lesion contrast, small task-contrast area) can be found in the bottom row of Fig. 4. The three metrics diverge, even at low task-contrast values, as the histogram of test-statistic measurements deviates from normal (quantile–quantile plots fit a linear model with  $r^2 = 0.9438$ .) Large deviations from normal show that ideal-observer performance, via  $\text{SNR}_I^2$  and  $d_A^2$ , are underestimated relative to task information. However,  $\text{SNR}_I^2$  is clearly more affected than  $d_A^2$ .

Equation (9) defines the task information contained in echo data, while (10) shows that we can measure this information using ideal-observer analysis from estimates of the probabilities of detection  $P_D$  and false alarm  $P_F$ . Although it is not immediately obvious how to design the best diagnostic system based on these results, there are clues. Performance is increased by providing observers with as many independent samples of the task as possible. This condition is achieved by increasing spatial resolution to minimize the echo-data correlation area, i.e.,

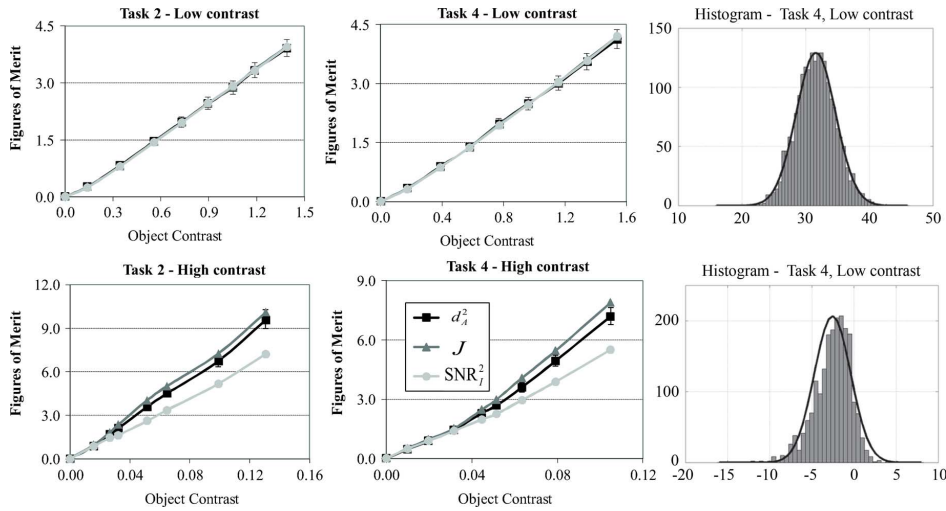


Fig. 4. Two experiments were conducted to compare the metrics  $J$ ,  $d_A^2$ , and  $\text{SNR}_I^2$  for Tasks 2 and 4. In all cases *task contrast*, i.e.,  $\Delta\mathbf{S}$ , was varied by the abscissas. However, in Exp. 1 (top row), *lesion contrast*,  $\max \mathbf{S}_0$ , within each image was set to a low value (10%) while the spatial extent of the feature was expanded to provide a task area larger than that of the data in Fig. 3. In Exp. 2 (bottom row), lesion contrast was set to a high value (99%) while the spatial extent of the feature was reduced to provide a task area much smaller than that of data in Fig. 3. The goal was to keep overall performance rough equivalent to the comparable data in Fig. 3. The upper right histogram is for the test-statistic of Task 4 from low lesion-contrast measurements, specifically  $q_0(\lambda)$ , along with a Gaussian curve having the same sample mean and variance. The lower right histogram is for the test statistic of Task 4 from high lesion-contrast measurements along with the same Gaussian curve. The legend applies to all plots, and error bars denote one standard error. Note that the range of object contrast changes between plots to draw the reader's attention to differences.

produce fine speckle patterns. Task features clearly stand out from the noise as contrast resolution and echo SNR increase. In a companion paper, we discover how these features manifest as coupled instrument parameters that may be adjusted to maximize diagnostic performance.

## V. CONCLUSION

A designer's goal is to maximize observer performance. We found that the contrast mechanism of an imaging modality will fundamentally influence the ideal observer's strategy and performance. In sonography, where the test statistic  $\lambda(\mathbf{g})$  is a quadratic function of the echo signal  $\mathbf{g}$ ,  $\lambda$  can have a non-normal distribution for small-area discrimination tasks. Yet, even for the high-contrast boundary-discrimination problems examined, class separability in the recorded RF echo data, as measured by  $J$ , closely approximates ideal performance via  $d_A^2$ . However the deviation of  $\text{SNR}_I^2$  from  $d_A^2$  and  $J$  was significant. We conclude that the assessment of sonographic quality should be based on  $d_A^2$  or its surrogate  $J$  but not on  $\text{SNR}_I^2$ .

In a companion paper [15], we derive the *acquisition information spectrum* (AIS) for sonography from a spatial frequency expansion of  $J$  in a manner analogous to the *generalized noise equivalent quanta* (GNEQ) spectrum that has been so useful for designing radiographic systems [7]. AIS describes how instrument properties couple to clinical task spectra to predict ideal performance.

## APPENDIX A

### RELATION OF $J$ TO THE AREA BETWEEN DETECTION AND FALSE-ALARM CURVES

This appendix derives (10) that relates the  $J$  to the area between the detection and false-alarm probability curves as func-

tions of the decision threshold. Integrating by parts the right-hand side of (10) provides us

$$\int_{-\infty}^{\infty} dt \{P_D(t) - P_F(t)\} = t \{P_D(t) - P_F(t)\} \Big|_{-\infty}^{\infty} - \int_{-\infty}^{\infty} t d\{P_D(t) - P_F(t)\}. \quad (\text{A1})$$

To evaluate the first term on the right-hand side of (A1), we apply the Chernoff bound under the assumption of finite moments to obtain [30]

$$P_D(t) = \Pr(\lambda(\mathbf{g}) > t | i = 1) < e^{-\beta t} M_1(\beta) \text{ for } \beta > 0 \quad (\text{A2})$$

where  $M_i(\beta)$  is the moment-generating function for the  $i$ th class of data, given by [6]

$$M_i(\beta) = \int_{-\infty}^{\infty} d\lambda q_i(\lambda) \exp(\beta\lambda) \text{ for } i = 0, 1 \quad (\text{A3})$$

in which  $q_i(\lambda)$  is the pdf of the test statistic  $\lambda(\mathbf{g})$  underlying class  $i$ .

For  $t \rightarrow +\infty$ ,  $te^{-\beta t} \rightarrow 0$  since the decrease in  $e^{-\beta t}$  is much faster than the increase in  $t$ ,  $M_1(\beta)$  remains unchanged, therefore,  $tP_D(t) \rightarrow 0$ . Similarly,  $tP_F(t) \rightarrow 0$ , and  $t\{P_D(t) - P_F(t)\} \rightarrow 0$  as  $t \rightarrow +\infty$ .

For  $t \rightarrow -\infty$ , by changing variable  $t$  to  $t' = -t$ , the first term on the right-hand side of (A1) can be written as

$$t\{P_D(t) - P_F(t)\} = t' \{ \Pr(-\lambda(\mathbf{g}) > t' | H_1) - \Pr(-\lambda(\mathbf{g}) > t' | H_0) \}. \quad (\text{A4})$$

By noting that  $-\lambda(\mathbf{g}) = \ln(p_0(\mathbf{g})/p_1(\mathbf{g}))$  is also a log likelihood ratio and  $t' \rightarrow +\infty$ , therefore, the Chernoff bound still can be applied to  $-\lambda(\mathbf{g})$  and  $t'$ . Hence, we have  $t\{P_D(t) - P_F(t)\} \rightarrow 0$  as  $t \rightarrow -\infty$ .

Thus, there is only the second term left in right-hand side of (A2). Combining with

$$\frac{dP_D(t)}{dt} = -q_1(t) \quad \text{and} \quad \frac{dP_F(t)}{dt} = -q_0(t) \quad (\text{A-5})$$

the right-hand side of (A1) becomes

$$\begin{aligned} & - \int_{-\infty}^{\infty} t d\{P_D(t) - P_F(t)\} \\ &= \int_{-\infty}^{\infty} dt t [q_1(t) - q_0(t)] \\ &= \int_{-\infty}^{\infty} d\lambda \lambda [q_1(\lambda) - q_0(\lambda)] \end{aligned} \quad (\text{A6})$$

in which the last expression is obtained by changing the variable in the integral from  $t$  to  $\lambda$ . Because  $q_i(\lambda)$  is the density conditioned on the data class  $i$  being true, the integral can be written as

$$\begin{aligned} & \int_{-\infty}^{\infty} d\lambda \lambda [q_1(\lambda) - q_0(\lambda)] = E_1\{\lambda\} - E_0\{\lambda\} \\ &= \int d\mathbf{g} p_1(\mathbf{g}) \ln \left( \frac{p_1(\mathbf{g})}{p_0(\mathbf{g})} \right) - \int d\mathbf{g} p_0(\mathbf{g}) \ln \left( \frac{p_1(\mathbf{g})}{p_0(\mathbf{g})} \right). \end{aligned} \quad (\text{A7})$$

Combined with the definition of  $J$  in (9), we obtain (10).

#### APPENDIX B RELATION BETWEEN $J$ AND MOMENTS OF $\lambda$

In this section, we relate  $J$  to the moments of the log likelihood ratio  $\lambda$  under a normal distribution for  $q_0(\lambda)$ . We invoke the *exponential family of distributions*  $p_\tau(\mathbf{g})$  [31]

$$p_\tau(\mathbf{g}) = \frac{p_0(\mathbf{g})e^{\tau\lambda(\mathbf{g})}}{M_0(\tau)} \quad (\text{B1})$$

for  $0 \leq \tau \leq 1$ .  $M_0(\tau)$  is defined as the moment-generating function for  $i = 0$  [6], but in (B1) it serves as a normalization constant for pdf  $p_\tau(\mathbf{g})$ .

Denoting  $q_\tau(\lambda)$  as another exponential family for  $\lambda$  underlying each  $p_\tau(\mathbf{g})$  for data  $\mathbf{g}$ , it can be shown that if  $q_0(\lambda)$  is normally distributed, all distributions of  $q_\tau(\lambda)$  are necessarily normally distributed with the same variance [6].

The moment-generating function  $M_\tau(\beta)$  underlying  $p_\tau(\mathbf{g})$  can be written as

$$\begin{aligned} M_\tau(\beta) &= \int_{-\infty}^{\infty} d\mathbf{g} p_\tau(\mathbf{g}) e^{\beta\lambda(\mathbf{g})} \\ &= \frac{M_0(\beta + \tau)}{M_0(\tau)} \end{aligned} \quad (\text{B2})$$

in which the second expression is obtained by combining with (B1). The corresponding characteristic function for  $\lambda$  is

$$\psi_\tau(\xi) = \int_{-\infty}^{\infty} d\mathbf{g} p_\tau(\mathbf{g}) e^{-2\pi i \xi \lambda(\mathbf{g})}. \quad (\text{B3})$$

Comparing (A3) and (B3) gives us

$$M_\tau(\beta) = \psi_\tau \left( \frac{i\beta}{2\pi} \right). \quad (\text{B-4})$$

Replacing  $\beta = -2\pi i \xi$  and combining with (B4), we obtain

$$\psi_\tau(\xi) = \frac{1}{M_0(\tau)} \psi_0 \left( \xi + \frac{i\tau}{2\pi} \right). \quad (\text{B5})$$

Taking the inverse Fourier transform of (B5), we have

$$q_\tau(\lambda) = \frac{e^{\tau\lambda}}{M_0(\tau)} q_0(\lambda), \quad 0 \leq \tau \leq 1. \quad (\text{B6})$$

(B6) shows a relation among distributions of family  $q_\tau(\lambda)$ . Let  $\lambda$  given  $i = 0$  have a normal density

$$q_0(\lambda) = \frac{1}{\sqrt{2\pi\sigma_0}} e^{-(\lambda - \bar{\lambda}_0)^2 / 2\sigma_0^2} \quad (\text{B7})$$

where  $\bar{\lambda}_0 = E_0\{\lambda\}$  and  $\sigma_0^2 = \text{var}_0\{\lambda\}$  are the mean and variance. Substituting (B7) into (B6), we have

$$q_\tau(\lambda) = \frac{e^{\tau\bar{\lambda}_0 + \tau^2\sigma_0^2/2}}{M_0(\tau)} \frac{1}{\sqrt{2\pi\sigma_0}} e^{-(\lambda - \bar{\lambda}_0 - \tau\sigma_0^2)^2 / 2\sigma_0^2} \quad (\text{B8})$$

where  $M_0(\tau) = e^{\tau\bar{\lambda}_0 + \tau^2\sigma_0^2/2}$  is a moment generating function [2]. Thus,  $q_\tau(\lambda)$  is also normal with variance  $\sigma_0^2$ .

This result is consistent with the findings of Barrett *et al.* [6]; it describes a general property of any distribution in the family of  $\{q_\tau(\lambda) : 0 \leq \tau \leq 1\}$  including  $q_1(\lambda)$ .

To derive (12), we apply the *cumulant-generating function*  $L_0(\tau) = \ln M_0(\tau)$  [2], [6]. Taking its first derivative we obtain

$$\begin{aligned} L_0'(\tau) &= \frac{M_0'(\tau)}{M_0(\tau)} \\ &= \frac{1}{M_0(\tau)} \int_{-\infty}^{\infty} d\mathbf{g} \lambda(\mathbf{g}) p_0(\mathbf{g}) e^{\tau\lambda(\mathbf{g})}. \end{aligned} \quad (\text{B9})$$

Combining with (B1), the second expression in (B9) is recognized as  $\bar{\lambda}_\tau$ , the conditional mean of  $\lambda$  underlying  $p_\tau(\mathbf{g})$  [6]. By denoting  $\theta(\tau) = L_0'(\tau)$ , we obtain

$$\theta(\tau) = \bar{\lambda}_\tau = \frac{M_0'(\tau)}{M_0(\tau)}. \quad (\text{B10})$$

Taking the derivative of (B10), we have

$$\begin{aligned} \theta'(\tau) &= \frac{M_0''(\tau)}{M_0(\tau)} - \left( \frac{M_0'(\tau)}{M_0(\tau)} \right)^2 \\ &= \frac{1}{M_0(\tau)} \int_{-\infty}^{\infty} d\mathbf{g} \lambda^2(\mathbf{g}) p_0(\mathbf{g}) e^{\tau\lambda(\mathbf{g})} \\ &\quad - \bar{\lambda}_\tau^2. \end{aligned} \quad (\text{B11})$$

The integral in (B11) is the second moment of  $\lambda(\mathbf{g})$  given  $p_\tau(\mathbf{g})$ . Therefore

$$\theta'(\tau) = \text{var}_\tau(\lambda) = \sigma_0^2. \quad (\text{B12})$$

Equation (B12) means that  $\theta'(\tau) > 0$  for  $0 \leq \tau \leq 1$  or  $\theta(\tau)$  is a continuous and strictly monotonic function in that range

of 0 to  $\tau$ . We define the Kullback–Leibler divergence  $J(0, \tau)$  between  $p_\tau(\mathbf{g})$  and  $p_0(\mathbf{g})$  as

$$\begin{aligned} J(0, \tau) &= \int (p_\tau(\mathbf{g}) - p_0(\mathbf{g})) \ln \frac{p_\tau(\mathbf{g})}{p_0(\mathbf{g})} d\mathbf{g} \\ &= (\theta(\tau) - \theta(0))\tau. \end{aligned} \quad (\text{B13})$$

At  $\tau = 1$ ,  $J(0, 1) = J$ , the divergence defined in (9).

From (B13),  $J(0, \tau)$  is also considered as a function of  $\theta$ . Denoting  $J(0, \tau) = m(\theta)$ , we apply a second-order Taylor series expansion of  $m(\theta)$  at  $\theta(0)$  to obtain

$$\begin{aligned} m(\theta) &= m(\theta(0)) + (\theta(\tau) - \theta(0))m'(\theta(0)) \\ &\quad + \frac{1}{2}(\theta(\tau) - \theta(0))^2 m''(\theta(\xi)) \end{aligned} \quad (\text{B14})$$

where  $\xi$  is some value between 0 and  $\tau$ . The last term of (B14) is obtained by combining with the property of  $\theta(\tau)$  which is continuous and strictly monotonic in the range of  $[0, \tau]$ . Derivatives of  $m(\theta)$  are given by

$$\begin{aligned} m'(\theta) &= \tau(\theta) + (\theta(\tau) - \theta(0))\tau'(\theta) \\ m''(\theta) &= 2\tau'(\theta) + (\theta(\tau) - \theta(0))\tau''(\theta). \end{aligned} \quad (\text{B15})$$

With  $\theta'(\tau)\tau'(\theta) = 1$ , we take the derivative of both sides to have  $\theta''(\tau)\tau'(\theta) + \theta'(\tau)\tau''(\theta) = 0$ . Since  $\theta'(\tau) = \sigma_0^2$  is a constant,  $\theta''(\tau) = 0$  so that  $\tau''(\theta) = 0$  and the second line of (B15) becomes

$$m''(\theta(\tau)) = \frac{2}{\theta'(\tau)} = \frac{2}{\sigma_0^2}. \quad (\text{B16})$$

Evaluating other derivatives of  $m(\theta(\tau))$  at  $\tau = 0$ , we have

$$\begin{aligned} m(\theta(0)) &= 0 \\ m'(\theta(0)) &= \tau(\theta) = 0. \end{aligned} \quad (\text{B17})$$

Thus  $m(\theta)$  or  $J(0, \tau)$  in (B13) is simplified to

$$J(0, \tau) = \frac{[\theta(\tau) - \theta(0)]^2}{\sigma_0^2}. \quad (\text{B18})$$

At  $\tau = 1$ , we have

$$J(0, 1) = \frac{[\theta(1) - \theta(0)]^2}{\sigma_0^2}. \quad (\text{B19})$$

With  $J = J(0, 1)$ ,  $\sigma_0^2 = \sigma_1^2$ , and  $\theta(\tau) = \bar{\lambda}_\tau$ , we obtain (12).

#### REFERENCES

- [1] R. F. Wagner, "Low contrast sensitivity of radiologic, CT, nuclear medical, and ultrasound medical imaging systems," *IEEE Trans. Med. Imag.*, vol. 2, no. 3, pp. 105–121, Sep. 1983.
- [2] H. H. Barrett and K. J. Myers, *Foundations of Image Science*. Hoboken, NJ: Wiley, 2004.
- [3] R. F. Wagner and D. G. Brown, "Unified SNR analysis of medical imaging systems," *Phys. Med. Biol.*, vol. 30, pp. 489–518, 1985.
- [4] H. H. Barrett, "Objective assessment of image quality: Effects of quantum noise and object variability," *J. Opt. Soc. Am. A*, vol. 7, no. 7, pp. 1266–1278, 1990.
- [5] H. H. Barrett, J. L. Denny, R. F. Wagner, and K. J. Myers, "Objective assessment of image quality. II. Fisher information, Fourier crosstalk, and figures of merit for task performance," *J. Opt. Soc. Am. A*, vol. 12, pp. 834–852, 1995.
- [6] H. H. Barrett, C. K. Abbey, and E. Clarkson, "Objective assessment of image quality. III. ROC metrics, ideal observers, and likelihood-generating functions," *J. Opt. Soc. Am. A*, vol. 15, no. 6, pp. 1520–1535, 1998.
- [7] Medical imaging—The assessment of image quality ICRU Rep. 54, 1996.
- [8] S. W. Smith, R. F. Wagner, J. M. Sandrik, and H. Lopez, "Low contrast detectability and contrast/detail analysis in medical ultrasound," *IEEE Trans. Son. Ultrason.*, vol. 30, no. 3, pp. 164–173, May 1983.
- [9] G. E. Trahey, J. W. Allison, S. W. Smith, and O. T. v. Ramm, "A quantitative approach to speckle reduction via frequency compounding," *Ultrason. Imag.*, vol. 8, no. 3, pp. 151–164, Jul. 1986.
- [10] R. F. Wagner, M. F. Insana, and S. W. Smith, "Fundamental correlation lengths of coherent speckle in medical ultrasonic images," *IEEE Trans. Ultrason. Ferroelectr. Freq. Control*, vol. 35, no. 1, pp. 34–44, Jan. 1988.
- [11] J. M. Thijssen, B. J. Oosterveld, and R. F. Wagner, "Gray level transforms and lesion detectability in echographic images," *Ultrason. Imag.*, vol. 10, no. 3, pp. 171–195, Jul. 1988.
- [12] C. K. Abbey, R. J. Zemp, J. Liu, K. K. Lindfors, and M. F. Insana, "Observer efficiency in discrimination tasks simulating malignant and benign breast lesions with ultrasound," *IEEE Trans. Med. Imag.*, vol. 25, no. 2, pp. 198–209, Feb. 2006.
- [13] C. K. Abbey, N. Q. Nguyen, and M. F. Insana, "Optimal beamforming in ultrasound using the ideal observer," *IEEE Trans. Ultrason. Ferroelectr. Freq. Control*, vol. 57, no. 8, pp. 1782–1796, Aug. 2010.
- [14] N. Q. Nguyen, C. K. Abbey, and M. F. Insana, "An adaptive filter to approximate the bayesian strategy for sonographic beamforming," *IEEE Trans. Med. Imag.*, vol. 30, no. 1, pp. 28–37, Jan. 2011.
- [15] N. Q. Nguyen, C. K. Abbey, and M. F. Insana, "Objective assessment of sonographic quality II. Acquisition information spectrum," *IEEE Trans. Med. Imag.*, vol. 32, no. 4, pp. 691–698, Apr. 2013.
- [16] Breast Imaging Reporting and Data System Atlas Am. Coll. Radiol., Reston, VA, 2003.
- [17] R. J. Zemp, C. K. Abbey, and M. F. Insana, "Linear system model for ultrasonic imaging: Application to signal statistics," *IEEE Trans. Ultrason. Ferroelectr. Freq. Control*, vol. 50, no. 6, pp. 642–654, Jun. 2003.
- [18] J. A. Jensen and N. B. Svendsen, "Calculation of pressure fields from arbitrarily shaped, apodized, and excited ultrasound transducers," *IEEE Trans. Ultrason. Ferroelectr. Freq. Control*, vol. 39, no. 2, pp. 262–267, Mar. 1992.
- [19] J. A. Jensen, "Field: A program for simulating ultrasound systems," *Med. Biol. Eng. Comp.*, vol. 34, pp. 351–353, 1996.
- [20] S. S. Brunke, M. F. Insana, J. J. Dahl, C. Hansen, M. Ashfaq, and H. Ermert, "An ultrasound research interface for a clinical system," *IEEE Trans. Ultrason. Ferroelectr. Freq. Control*, vol. 54, no. 1, pp. 198–210, Jan. 2007.
- [21] S. Fields and F. Dunn, "Correlation of echographic visualizability of tissue with biological composition and physiological state," *J. Acoust. Soc. Am.*, vol. 54, no. 3, pp. 809–812, Sep. 1973.
- [22] M. F. Insana and D. G. Brown, "Acoustic scattering theory applied to soft biological tissues," in *Ultrasonic Scattering in Biological Tissues*, K. Shung and G. A. Thiemes, Eds. Boca Raton, FL: CRC Press, 1993.
- [23] R. F. Wagner, M. F. Insana, and D. G. Brown, "Statistical properties of radio-frequency and envelope-detected signals with applications to medical ultrasound," *J. Opt. Soc. Am. A*, vol. 4, no. 5, pp. 910–922, May 1987.
- [24] R. F. Wagner and H. H. Barrett, "Quadratic tasks and the ideal observer," *Proc. SPIE*, vol. 767, pp. 306–309, 1987.
- [25] D. M. Green and J. A. Swets, *Signal Detection Theory and Psychophysics*. Los Altos, CA: Peninsula, 1988.
- [26] D. Middleton, *An Introduction to Statistical Communication Theory*. New York: McGraw-Hill, 1960.
- [27] R. Shaw, "The equivalent quantum efficiency of the photographic process," *J. Photograph. Sci.*, vol. 11, pp. 199–204, 1963.
- [28] S. Kullback and R. A. Leibler, "On information and sufficiency," *Ann. Math. Stat.*, vol. 22, no. 1, pp. 79–86, 1951.
- [29] B. Efron and R. J. Tibshirani, *An Introduction to the Bootstrap*. New York: Chapman Hall, 1993.
- [30] H. V. Poor, *An Introduction to Signal Detection and Estimation*. New York: Springer-Verlag, 1994.
- [31] S. Kullback, *Information Theory and Statistics*. New York: Dover, 1997.